Efficient single-photon emission via quantum-confined charge funneling to quantum dots

Oleg Mitrofanov

o.mitrofanov@ucl.ac.uk

University College London https://orcid.org/0000-0003-3510-2675

Sanghyeok Park

Sandia National Laboratories

Kalifa Rahman

Sandia National Laboratories

Darryl Shima

University of New Mexico

Ganesh Balakrishnan

University of New Mexico

Jaeyeon Yu

Sandia National Laboratories

Hyunseung Jung

Sandia National Laboratories

Jasmine Mah

Sandia National Laboratories

Samuel Prescott

University College London https://orcid.org/0009-0003-5256-3075

Pingping Chen

University of Virginia, Charlottesville

Sadhvikas Addamane

Sandia National Laboratories

Douglas Pete

Sandia National Laboratories

Andrew Mounce

Sandia National Laboratories https://orcid.org/0000-0002-8115-2764

Ting Luk

Sandia National Laboratories

Prasad Iyer

Sandia National Laboratories https://orcid.org/0000-0002-6898-3619

Igal Brener

Sandia National Laboratories https://orcid.org/0000-0002-2139-5182

Article

Keywords:

Posted Date: April 3rd, 2025

DOI: https://doi.org/10.21203/rs.3.rs-6222330/v1

Additional Declarations: There is **NO** Competing Interest.

Abstract

Quantum light sources, particularly single-photon emitters (SPEs), are critical for quantum communications and computing. Among them, III-V semiconductor quantum dots (QDs) have demonstrated superior SPE metrics, including near-unity brightness, high photon purity, and indistinguishability, making them especially suitable for quantum applications. However, their overall quantum efficiency — determined by a product of the internal, excitation, and out-coupling efficiencies — remains limited, primarily due to low (typically below 0.1%) excitation efficiency. This has hindered their applications in quantum information systems, including for multi-photon cluster state generation and Boson sampling. To mitigate the low excitation efficiency, here we realized liquid droplet etched GaAs QDs in a microscale 3D AlGaAs charge-carrier funnel using molecular beam epitaxy. The funnel channels charge carriers to the QD and enhances the overall emission efficiency by over one order of magnitude while preserving the SPE behavior. We reveal that a modified energy landscape around the QD leads to the excitation efficiency improvement. These energy landscape-modified QDs can be operated with optical excitation up to 10 μm away from the QD, raising the promise of efficient and scalable electrically driven epitaxial QD SPE for quantum information systems.

Introduction

Quantum light sources and specifically single-photon emitters (SPEs) have become the key enabling component for quantum communications and quantum computing [1-4]. A multitude of SPEs ranging from cold atoms [5,6] to defects in solids [7-9] and 2D materials [10,11] have been developed to provide the single-photon source functionality. Among them, III-V group semiconductor quantum dots (QDs) [12,13] represent one of the most established SPEs, and their use has evolved recently from initial proof-of-principle demonstrations (e.g. generation of photon-number states [14] and cluster states [15,16]) to practical deployment in quantum computing processors [17].

Semiconductor QD-based SPEs have shown some of the best metrics for quantum computing [1,4]: close to unity brightness [18, 19], high photon purity [14,16,17,20] and near unity indistinguishability [16, 17, 19, 21]. They also hold high potential for scalability and integration, and for on-demand electrical driving [22-26]. However, the best SPE performance so far has relied on resonant optical pumping of QDs, which requires sophisticated filtering techniques [27-33] and highly fine tuning of the excitation laser limiting the scalability of the approach. Non-resonant optical pumping, and ultimately electrical driving, simplify the filtering of photons, but these approaches tend to generate parasitic charge carriers and phonons near the QD, leading to faster dephasing and deterioration of the photon indistinguishability [4, 12]. Furthermore, the overall quantum efficiency, i.e. the number of pump photons or injected charge carriers required to produce a photon in the single-photon state, is far from the desired value of unity. This low overall quantum efficiency presents a major roadblock for quantum computation limiting the operation rate, the efficiency of multi-photon cluster state generation, and the number of demultiplexing channels in Boson sampling [16, 17, 21].

Here, we demonstrate a solution to the low overall QD efficiency problem by developing a material-based microscale 3D charge-carrier funnel for QDs grown by molecular beam epitaxy (MBE). In a single MBE process, we realized a unique combination of an *in situ* nanoscale GaAs QD and a microscale AlGaAs charge-carrier funnel. The funnel forms an attractive potential, which channels the charge carriers injected within the microscale volume toward the embedded GaAs QDs, increasing the overall quantum efficiency by over one order of magnitude compared to ordinary QDs (o-QDs) in the same sample. Using nanoscale structural analysis and photo-luminescence (PL) imaging, we reveal that the enhancement in efficiency originates from a modified energy landscape around the QD, which is determined by the material composition and the effect of quantum confinement within the funnel. We demonstrate that these *energy landscape modified* (ELM) QDs operate as SPEs making them attractive as light sources for quantum applications. The ELM QDs also enable a regime of remote QD excitation, where charge carriers are injected microns away from the QD, raising the potential for realizing efficient electrically driven on-demand SPEs built on a scalable platform [34, 35].

For a single QD, the overall quantum efficiency h is a product of the internal quantum efficiency h_{int}, the probability of emitting a photon when the QD is in the excited state, as well as the excitation and the out-coupling efficiencies, h_x and h_{oc} : $h = h_{int}h_xh_{oc}$. The *internal* quantum efficiency h_{int} is already close to unity for semiconductor QDs [36,37], while the out-coupling efficiency h_{oc} can be engineered to approach unity by introducing cavities, resonators and metasurfaces [38-43], which modify the photonic environment around the QD and influence the out-coupling, directivity, as well as the spontaneous emission rate via the Purcell effect. In stark contrast, the excitation quantum efficiency h_x typically stays below 0.1%, resulting in considerable losses of pump power during optical excitation. Furthermore, compensation of the low excitation efficiency with higher pump power deteriorates the SPE properties due to the parasitic charge carriers and phonons near the QD.

The problem of low excitation efficiency is mitigated here using the concept of ELM-QD illustrated in Fig. 1a: the GaAs QD is located in a low aluminum (Al) fraction (~20% Al) AlGaAs micrometer-scale disk, which serves as a charge-carrier funnel within a higher Al fraction (~40% Al) AlGaAs barrier layer. The bandgap energy in the disk is lower than the bandgap energy in the barrier, varying gradually between the two levels due to the quantum confinement effect (Fig. 1b). Charge carriers within a microscale volume surrounding the QD therefore can be *stored* and *funneled* to the QD.

To realize this concept using MBE, where the formation of 3D structures, such as QDs, quantum rings [44, 45] and nanowires [46], requires special growth conditions, we introduce a process of Ga droplet crystallization which forms an AlGaAs disc, just before the growth of QDs. First, during the growth of the $Al_{0.4}Ga_{0.6}As$ barrier layer, a Ga droplet is deposited on its surface (Fig. 1c). The droplet then crystallizes into AlGaAs by reacting with incoming aluminum and arsenic (As). Due to the energetics of the MBE growth process, AlGaAs exhibits preferential crystallization along (110) directions, transforming the droplet into a microscale AlGaAs disk [47]. The Al composition in the disk is ~20%, lower than that in the barrier layer. After the disk has fully crystallized, GaAs QDs are grown using the liquid droplet etched

(LDE) process with Al droplets, with only a few dots being etched into and grown inside the AlGaAs disk. Finally, the disk and the QDs are covered with a barrier layer of $Al_{0.4}Ga_{0.6}As$ (Fig. 1c).

As a result of this growth process, we form QDs in two energetically different environments: o-QDs are located in the $Al_{0.4}Ga_{0.6}As$ barrier and ELM-QDs are located inside the sparsely distributed $Al_{0.2}Ga_{0.8}As$ disks, serving as the charge-carrier funnels illustrated in Fig. 1c. The difference between the two kinds of QDs is striking, as evident in PL images of the sample, where the ELM-QDs show over one order of magnitude higher photon emission compared to the o-QDs (Fig. 1d).

To reveal the nanoscale structure of the AlGaAs charge carrier funnel containing the QDs, we examined them with cross-sectional transmission electron microscopy (TEM). In Fig. 2, four layers can be distinguished in a TEM image of a representative funnel (Fig. 2a), thanks to the clear contrast in brightness caused by variation in the Al composition between the layers. The bottom $Al_{0.7}Ga_{0.3}As$ sacrificial layer has the darkest shade due to the highest Al content. Above it, is a lighter gray ~30-nm-thick barrier $Al_{0.4}Ga_{0.6}As$ layer. The AlGaAs funnel, which has the lightest tone corresponding to the lowest Al content, is located above it. The thickness of this layer varies in the image from 10-20 nm at the edges to approximately 150 nm at the center of the funnel. Finally, another medium-gray $Al_{0.4}Ga_{0.6}As$ barrier layer caps the heterostructure. The funnel is fully contained within the $Al_{0.4}Ga_{0.6}As$ barrier. An atomic force microscopy topographical image of an area near a typical funnel is shown in Fig. 2d. It displays a disk of ~8 mm in diameter, with a smaller partial ring-shaped ridge (~1-2 mm) at the center.

Higher magnification TEM images show the evidence of LDE GaAs QDs formed just above the ridges within the AlGaAs funnel (Fig. 2b). The QDs can be identified by thin dark streaks (high Al composition) only a few nm above the top interface of the AlGaAs ridges. The streaks appear where the TEM section sliced through thin Al 'puddles,' which form around QDs [48], whereas the QDs themselves are not visible. Nevertheless, since LDE QD are located below the puddles (Fig. 1b), the QDs are likely to be inside the AlGaAs charge-carrier funnel, ~1-10 nm below the streaks. We note that the LDE QDs are preferentially formed on the ridge slopes, close to the region where the $Al_{0.2}Ga_{0.8}As$ disk thickness is highest. This occurs due to the growth energetics of LDE QDs which preferentially form along the (110) facets [47].

The low Al composition in the funnel provides the lowest potential energy for charge carriers and excitons, and it therefore can attract them to the QD. To evaluate the corresponding energy landscape near the QDs quantitatively, we performed the energy dispersive X-ray spectroscopy (EDS) and mapped the elemental composition in and near the funnel, along line scans A and B (Fig. 2c). The Al composition in the AlGaAs barrier (blue regions) is ~40%, whereas it drops down to ~20% in the funnel (pink region). Using the funnel's elemental composition and its geometry, we calculate the conduction band energy and the quantum confinement energy within it. The corresponding energy profile is shown in Fig. 2e and it resembles that of an in-plane potential well with a parabolic profile. Although the composition within the funnel is uniform, the confinement energy for electrons increases gradually near the edges where the disk thickness decreases. The energy eventually approaches the conduction band level in the barrier. A similar energy landscape is experienced by the holes. As a result, the photoexcited charge carriers are

attracted and funneled toward the funnel center, where QDs are preferentially formed, close to the ridges (the lowest potential energy). We note that the quantum confinement energy for an $Al_{0.2}Ga_{0.8}As$ layer thicker than ~50 nm is small, <1.7 meV, and it only weakly depends on the thickness. It therefore makes the energy landscape relatively flat near the funnel center (Fig. 2e).

The energy landscape in the vicinity of the QDs becomes experimentally evident in a PL spectral map measured along a line scan through an ELM-QD (Figure 3a): at the map center is the QD with a series of spectral lines corresponding to QD exciton states (left panel). In the energy region above the QD exciton emission, one can observe a broad PL peak continuously changing its energy along the line scan, with the lowest energy point close to the QD location. As the distance from the QD increases the peak gradually shifts to higher energies following an inverted bell-shape trace in the map. This PL peak represents the bandgap energy within the funnel. As the $Al_{0.2}Ga_{0.8}As$ disk becomes thinner towards the edges, the PL peak energy shifts to the exciton energy in $Al_{0.4}Ga_{0.6}As$ (Supplementary Information S1), and the shift is consistent with the calculations of the quantum confinement energy within the funnel (Fig. 2e).

This modified energy landscape facilitates the capture and channeling of photoexcited charge carriers in its vicinity of the QD. We found that all investigated ELM-QDs displayed PL maps similar to the map in Fig. 3a, with some variation in the minimum bandgap energy. Examples of the PL spectral map are summarized in Fig. 3b and in Supplementary Information: the minimum exciton energy at the funnel center varied from ~250 meV to ~50 meV below the exciton energy in the barrier. The elemental uniformity observed in the EDS measurements (Fig. 2) suggests that the thickness variation, rather than a change in material composition, is the major factor defining the energy landscape. The disk thickness, and the corresponding quantum confinement energy, therefore provide a tuning knob for engineering the attractive potential near LDE QDs (Supplementary Information S1).

Next, we explore whether the modified energy landscape can be exploited for on-demand electrical pumping. As a step toward this goal, we consider *remote* optical excitation when a QD is not pumped directly but at a distance, with the photoexcited charge carriers requiring to travel micrometers to reach the QD. Such *remote* optical pumping could also reduce dephasing due thermal fluctuations caused by absorption of the pump beam. To investigate the potential for remote optical excitation, we monitored PL from ELM-QDs while exciting them with a focused optical beam at a variable distance, up to several micrometers away. Figure 3(d) summarizes the intensity of QD exciton emission as a function of the distance between the QD and the pump beam position. The ELM-QD continues emitting photons even when the pump beam is displaced ~5-10 mm away from the QD location, showing effective carrier funneling due to the modified energy landscape. In contrast, PL intensity for o-QDs drops dramatically when the pump beam is displaced from the dot by only 1-2 mm, a distance comparable to the width of the point-spread function in our PL imaging system. We note that this remote pumping has the potential of easing the fabrication precision requirement in nanometer-scale alignment of photonic cavities to QDs.

The charge-carrier funneling effect is most clearly evident in an increase in the overall efficiency for ELM-QDs compared to the o-QD, and it is summarized in Fig. 4 showing the PL intensity for the QDs excited at different optical pump powers. For the ELM-QD, a narrow linewidth peak emission at 1.80 eV (689 nm) increases linearly with the pump power first, then, at ~100 nW, the peak intensity saturates and starts decreasing, the linewidth broadens and additional lines due to exciton complexes appear [49-52] (see Supplementary Information S3). In contrast, the o-QD shows a gradual increase in PL intensity in the same range of the pump powers. In Fig. 4b, PL from the o-QD 1 is two orders of magnitude weaker than that from ELM-QD 1 at the pump power of 100 nW. PL intensity for ELM-QDs on average is one order of magnitude higher compared to that for o-QDs (at low excitation powers, see Supplementary Information S3), and the saturation power for the ELM-QDs is on average over one order of magnitude lower indicating an increased overall efficiency due to more efficient excitation. We also find that the excitation efficiency h_x for the ELM-QDs is in the range of 4-40 times higher than that for previously reported ordinary QDs [13, 39, 40, 53-58]. We note that this level of enhancement is comparable to the outcoupling enhancement achieved with photonic environment engineering [59] (Supplementary Information S4).

Most importantly, we found that ELM-QDs can serve as SPEs for quantum applications. Using a Hanbury-Brown-Twiss interferometer, we determined that the ELM-QD in Fig. 3a optically pumped at 50 nW displayed a single-photon emitter signature with a fast decay rate of 5.1 GHz (Fig. 4d). The faster decay rate compared to previously reported values [43] is likely to be originating from readily available charge carriers in the funnel, around the QD. The minimum of the second-order correlation function, $g^{(2)}(0) = 0.04$ was determined by including the random coincidence correlation correction [60] (Supplementary Information S5). The $g^{(2)}(0)$ measurement satisfies the criterium for single-photon emitter ($g^{(2)}(0) < 0.5$), and therefore the efficiency GaAs LDE QDs is increased without destroying their SPE properties.

In conclusion, we introduce and demonstrate a charge-carrier funnel for enhancing the overall quantum efficiency of GaAs LDE QDs. We engineered the in-plane energy landscape around the QD by leveraging the specially-grown microscale AlGaAs disks which attract and funnel excited charge carriers to the QDs, resulting in a significant increase in PL efficiency – over one order of magnitude greater than that of ordinary LDE GaAs QDs. These funnels can serve as effective charge carrier attractors and reservoirs enabling remote, up to 10 mm, optical excitation and promising an efficient and scalable material platform for electrically driven SPE QD emitters. This energy landscape engineering approach not only presents a practical means of improving QD-based single-photon emitter performance. We anticipate that together with photonic environment engineering, it will open new avenues for developing scalable quantum light sources that can be integrated into future quantum information systems [35, 42, 61, 62].

Methods

Material Growth: GaAs quantum dot (QD) samples were grown by molecular beam epitaxy on a GaAs (100) substrate. The epitaxial structure consists of (from bottom) a 300 nm thick GaAs smoothing layer, a 500 nm $Al_{0.75}Ga_{0.25}As$ sacrificial layer and a 140 nm $Al_{0.4}Ga_{0.6}As$ barrier layer protected on both sides with 5 nm thick GaAs layers, all grown at 600°C. Charge carrier funnels were formed from gallium

droplets, which were deposited throughout the growth. The probability of gallium droplet formation is higher for lower temperatures of the tip of the gallium effusion cell [63], and the tip:base temperature ratio of the cell was varied to favor the droplet formation. Droplets deposited ~ 20–30 nm into the growth of the $Al_{0.4}Ga_{0.6}As$ barrier form the charge carrier funnels. A sheet of low-density GaAs liquid droplet etched (LDE) QDs were embedded in the middle of the barrier layer. First, the growth process was paused and the substrate temperature was increased to 620°C under an arsenic soak; the excess arsenic on the surface was removed by annealing the substrate at this temperature for 40 s without any arsenic supply. Next, only aluminum was introduced to form droplets with a nominal thickness of 0.6 ML. Then the droplets were annealed in a low-arsenic environment for 300 s to promote etching of nanovoids. To form QDs in the voids, GaAs was deposited using migration-enhanced epitaxy followed by annealing for 300s. The Ga and Al growth rates were in the range of 0.4–0.5 ML/s. The As:Ga beam equivalent pressure ratio was maintained at 45–50 for most of the growth and reduced to ~7.5 for a low-arsenic environment.

Photoluminescence spectroscopy and imaging

Samples were cooled down to 10 K in the closed-loop Montana Instruments cryostat. A 520 nm wavelength laser diode was used for nonresonant optical excitation. The laser beam was focused using an microscope objective with the numerical aperture of 0.4. The laser beam spot diameter was 1 μm. Photoluminescence was collected through the same microscope objective and analyzed using a 50 cm length grating spectrometer equipped with a 600 and 1800 groove per millimeter gratings and a 1340 × 100 back illumination array detector (Teledyne Princeton instruments). A pair of superconducting nanowire single photon detectors (Quantum Opus) and a time-correlated single-photon counting module (Picoharp 300, Picoquant) were used for measuring the second-order correlation function. Scanning PL and correlation time tagging measurements were collected using pyscan (github.com/sandialabs/pyscan), an open-source measurement tool box developed at the Center of Integrated Nanotechnologies.

Declarations

Acknowledgement

This work was supported by the U.S. Department of Energy (DOE), Office of Basic Energy Sciences, Division of Materials Sciences and Engineering and by the EPSRC (EP/S022139/1), and performed, in part, at the Center for Integrated Nanotechnologies, an Office of Science User Facility operated for the U.S. DOE Office of Science. Sandia National Laboratories is a multi-mission laboratory managed and operated by National Technology and Engineering Solutions of Sandia, LLC., a wholly owned subsidiary of Honeywell International, Inc., for the U.S. DOE's National Nuclear Security Administration under contract DE-NA0003525. This paper describes objective technical results and analysis. Any subjective views or opinions that might be expressed in the paper do not necessarily represent the views of the U.S. DOE or the United States Government.

References

1. Aharonovich, I., Englund, D. & Toth, M. Solid-state single-photon emitters. *Nature Photon* 10, 631–641 (2016).
2. Madsen, L.S, et al. Quantum computational advantage with a programmable photonic processor. *Nature* 606, 75–81 (2022).
3. Lukin. D. M, Guidry. M. A. & Vuckovic. J, Integrated Quantum Photonics with Silicon Carbide: Challenges and Prospects. *PRX. Quantum* 1, 020102 (2020)
4. Senellart, P., Solomon, G. & White, A. High-performance semiconductor quantum-dot single-photon sources. *Nature Nanotech* 12, 1026–1039 (2017).
5. Darquié, B. et al. Controlled Single-Photon Emission from a Single Trapped Two-Level Atom. Science 309, 454-456(2005).
6. Maring, N. et al. Photonic quantum state transfer between a cold atomic gas and a crystal. *Nature* 551, 485–488 (2017).
7. Aharonovich, I, Neu, E., Diamond Nanophotonics. *Adv. Opt. Mat*, 2: 911-928. (2014)
8. Lukin, D.M., et al. 4H-silicon-carbide-on-insulator for integrated quantum and nonlinear photonics. *Nat. Photonics* 14, 330–334 (2020).
9. Lukin, D. M. et al. Two-Emitter Multimode Cavity Quantum Electrodynamics in Thin-Film Silicon Carbide Photonics. *Phys. Rev. X* 13, 011005 (2023).
10. Branny, A., et al. Deterministic strain-induced arrays of quantum emitters in a two-dimensional semiconductor. *Nat Commun* 8, 15053 (2017).
11. Luo, Y., et al. Deterministic coupling of site-controlled quantum emitters in monolayer WSe_2 to plasmonic nanocavities. *Nature Nanotech* 13, 1137–1142 (2018).
12. Somaschi, N., Giesz, V., De Santis, L. *et al.* Near-optimal single-photon sources in the solid state. *Nature Photon* **10**, 340–345 (2016).
13. Uppu, R., *et al.* Quantum-dot-based deterministic photon–emitter interfaces for scalable photonic quantum technology. *Nat. Nanotechnol.* **16**, 1308–1317 (2021)
14. Loredo, J.C., *et al.* Generation of non-classical light in a photon-number superposition. *Nat. Photonics* **13**, 803–808 (2019).
15. I. Schwartz. et al., Deterministic generation of a cluster state of entangled photons. *Science* 354, 434-437(2016).
16. Coste, N., *et al.* High-rate entanglement between a semiconductor spin and indistinguishable photons. *Nat. Photon.* **17**, 582–587 (2023).
17. Maring, N., *et al.* A versatile single-photon-based quantum computing platform. *Nat. Photon.* **18**, 603–609 (2024).
18. Gazzano, O., et al. Bright solid-state sources of indistinguishable single photons. *Nat Commun* 4, 1425 (2013)

19. Tomm, N., *et al.* A bright and fast source of coherent single photons. *Nat. Nanotechnol.* **16**, 399–403 (2021).
20. Zhai, L., et al. Low-noise GaAs quantum dots for quantum photonics. Nat Commun 11, 4745 (2020).
21. Wang. H., et al. Boson Sampling with 20 Input Photons and a 60-Mode Interferometer in a 10^{14}-Dimensional Hilbert Space. *Phys. Rev. Lett*. 123, 250503 (2019).
22. Yuan, Z et al. Electrically Driven Single-Photon Source. *Science* 295,102-105(2002).
23. Heindel, T et al. Quantum key distribution using quantum dot single-photon emitting diodes in the red and near infrared spectral range. *New J. Phys*. 14 083001 (2012)
24. Huang, H. et al. Electrically-Pumped Wavelength-Tunable GaAs Quantum Dots Interfaced with Rubidium Atoms. *ACS. Photonics* 4, 868-872 (2017)
25. Müller, T, et al. A quantum light-emitting diode for the standard telecom window around 1,550 nm. *Nat Commun* 9, 862 (2018)
26. Boretti, A. et al. Electrically Driven Quantum Light Sources. *Adv. Opt. Mat*. 3: 1012-1033. (2015)
27. Muller. A. et al., Resonance Fluorescence from a Coherently Driven Semiconductor Quantum Dot in a Cavity. *Phys. Rev. Lett*. 99, 187402 (2007).
28. Ates. S, et al., Post-Selected Indistinguishable Photons from the Resonance Fluorescence of a Single Quantum Dot in a Microcavity. *Phys. Rev. Lett*. 103, 167402 (2009)
29. Nguyen H. S. et al., Ultra-coherent single photon source. *Appl. Phys. Lett*. 99, 261904 (2011).
30. Ulhaq. A. et al., Cascaded single-photon emission from the Mollow triplet sidebands of a quantum dot. *Nat. Photonics* 6, 238 (2012)
31. Kuhlmann, A. V. et al. A dark-field microscope for background-free detection of resonance fluorescence from single semiconductor quantum dots operating in a set-and-forget mode. *Rev. Sci. Instrum*. 84, 073905 (2013).
32. Vamivakas, A., et al. Spin-resolved quantum-dot resonance fluorescence. *Nature Phys* 5, 198–202 (2009).
33. Vamivakas, A., et al. Observation of spin-dependent quantum jumps via quantum dot resonance fluorescence. *Nature* 467, 297–300 (2010).
34. Heindel. T, et al. Electrically driven quantum dot-micropillar single photon source with 34% overall efficiency, *Appl. Phys. Lett.* 96, 011107 (2010)
35. Boretti, A. et al. Electrically Driven Quantum Light Sources. *Adv. Opt. Mat*. 3: 1012-1033. (2015)
36. Chao, WC., et al. High efficiency green InP quantum dot light-emitting diodes by balancing electron and hole mobility. *Commun Mater* 2, 96 (2021).
37. Große, J, et al. Quantum efficiency and oscillator strength of InGaAs quantum dots for single-photon sources emitting in the telecommunication O-band. *Appl. Phys. Lett*. 119, 061103 (2021)
38. Solntsev, A.S., Agarwal, G.S. & Kivshar, Y.S. Metasurfaces for quantum photonics. *Nat. Photonics* 15, 327–336 (2021)

39. Reimer, M., et al. Bright single-photon sources in bottom-up tailored nanowires. *Nat Commun* 3, 737 (2012)
40. Claudon, J., et al. A highly efficient single-photon source based on a quantum dot in a photonic nanowire. *Nature Photon* 4, 174–177 (2010)
41. Lodahl, P., et al. Controlling the dynamics of spontaneous emission from quantum dots by photonic crystals. *Nature* 430, 654–657 (2004)
42. Heindel, T, et al, Quantum dots for photonic quantum information technology, *Adv. Opt. Photon*. 15, 613-738 (2023)
43. Iyer, P. P., et al. Control of Quantized Spontaneous Emission from Single GaAs Quantum Dots Embedded in Huygens' Metasurfaces. *Nano. Lett*. 24, 4749-4757. (2024)
44. Granados, D., Garcia, J. M. Customized nanostructures MBE growth: from quantum dots to quantum rings. *Journal of Crystal Growth* 251, 213-217 (2003)
45. Granados, D., Garcia, J. M. In(Ga)As self-assembled quantum ring formation by molecular beam epitaxy. *Appl. Phys. Lett*. 82, 2401-2403 (2003)
46. Wang. N., Cai. Y., Zhang. R. Q. Growth of nanowires, *Materials Science and Engineering: R: Reports* 60, 1-51 (2008)
47. Balakrishnan, G., et al. 2.0 μm wavelength InAs quantum dashes grown on a GaAs substrate using a metamorphic buffer layer. *Appl. Phys. Lett.* 84(12), 2058-2060 ((2004)
48. Zhang. Y et al. Unveiling the 3D Morphology of Epitaxial GaAs/AlGaAs Quantum Dots, *Nano Lett*. 24, 10106-10113 (2024)
49. Juska, G., et al. Towards quantum-dot arrays of entangled photon emitters. *Nature Photon* 7, 527–531 (2013).
50. Zieliński, M.et al. Excitonic complexes in natural InAs/GaAs quantum dots. *Phys. Rev. B*. 91,085303 (2015)
51. Abbarchi, M. et al. Energy renormalization of exciton complexes in GaAs quantum dots. *Phys. Rev. B*, 82, 201301 (2010)
52. Yu, Y. et al. Fundamental limits of exciton-exciton annihilation for light emission in transition metal dichalcogenide monolayers. *Phys. Rev. B*. 93, 201111 (2016)
53. Sapienza, L., et al. Nanoscale optical positioning of single quantum dots for bright and pure single-photon emission. *Nat Commun* 6, 7833 (2015).
54. Larocque, H., et al. Tunable quantum emitters on large-scale foundry silicon photonics. *Nat Commun* 15, 5781 (2024).
55. Li, X., et al. Bright semiconductor single-photon sources pumped by heterogeneously integrated micropillar lasers with electrical injections. *Light Sci Appl* 12, 65 (2023).
56. Gan, L, et al. Large-Scale, High-Yield Laser Fabrication of Bright and Pure Single-Photon Emitters at Room Temperature in Hexagonal Boron Nitride. *ACS Nano* 16, 9, 14254-14261 (2022)

57. Schlehahn, A, et al. Generating single photons at gigahertz modulation-speed using electrically controlled quantum dot microlenses. *Appl. Phys. Lett.* 108, 021104 (2016)
58. Wang, X.-J., et al. Enhanced brightness of quantum emitters via in situ coupling to the dielectric microsphere. *Appl. Phys. Lett*. 123, 133106 (2023)
59. Prescott, S, et. al. Mie metasurfaces for enhancing photon outcoupling from single embedded quantum emitters. *Nanophotonics*, (2024)
60. Brouri. R. et al., Photon antibunching in the fluorescence of individual color centers in diamond. *Opt. Lett*. 25, 1294 (2000)
61. Arakawa, Y, Holmes, M. J. Progress in quantum-dot single photon sources for quantum information technologies: A broad spectrum overview. *Appl. Phys. Rev*. 7, 021309. (2020)
62. F. Pelayo García de Arquer et al. Semiconductor quantum dots: Technological progress and future challenges. Science 373, eaaz8541(2021)
63. Romero, O. S., et al. Transmission electron microscopy-based analysis of electrically conductive surface defects in large area GaSb homoepitaxial diodes grown using molecular beam epitaxy. J. of Electron. Mat. 43, 926-930 (2014).

Figures

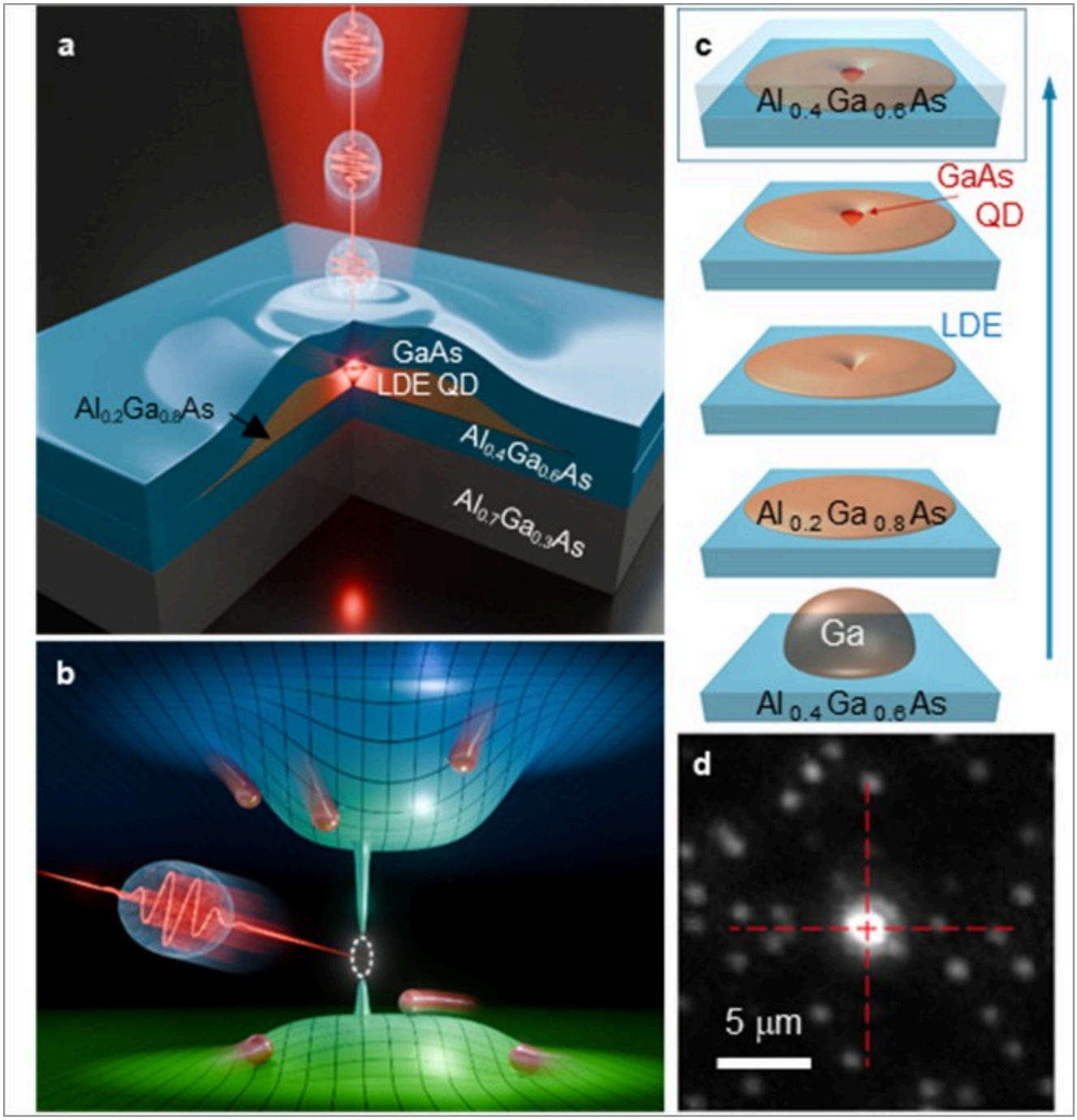

Figure 1

Quantum dot in charge carrier funnel. (a) Schematic of ELM-QD: an $Al_{0.2}Ga_{0.8}As$ disk (orange, acting as a charge carrier funnel) with a GaAs QD in the center. The disk attracts photoexcited charge carriers toward the QD inside the disk, increasing the efficiency of the QD. (b) Illustration of the conduction (top) and valence (bottom) band energy landscapes near the QD with electrons and holes funneled towards it. (c) Schematic diagram of the ELM-QD formation process during MBE growth. (d) Photoluminescence image of a sample area containing an ELM-QD (bright) at the center and o-QDs.

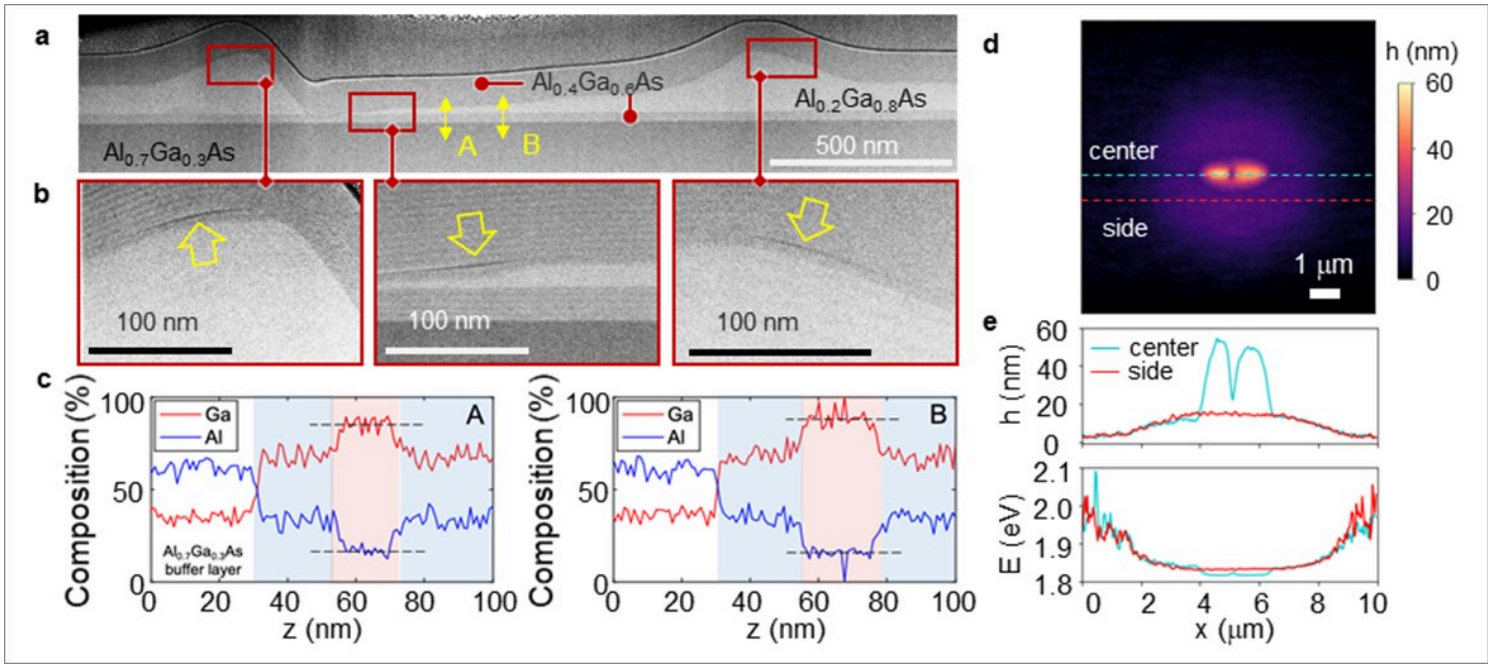

Figure 2

Nanoscale structure of ELM-QD. (a) Cross-sectional TEM image of a representative $Al_{0.2}Ga_{0.8}As$ funnel at 80,000X magnification. (b) Cross-sectional TEM images of LDE GaAs QDs at higher magnification (150,000 X, QD location in (a) is indicated with red boxes). Dark streaks (indicated with yellow arrows) show cross-sections of Al puddles formed near the QDs. (c) Ga and Al composition along line scans A and B in (a) obtained with EDS. The Ga (Al) composition is shown with the red (blue) line. (d) Atomic force microscopy (AFM) image of a typical ELM-QD. (e) Topography and the corresponding bandgap energy profile along two AFM line scans indicated by the blue and red dashed lines in (d). Bandgap energy in the funnel calculated using the AlGaAs disk thickness profiles and the Al composition.

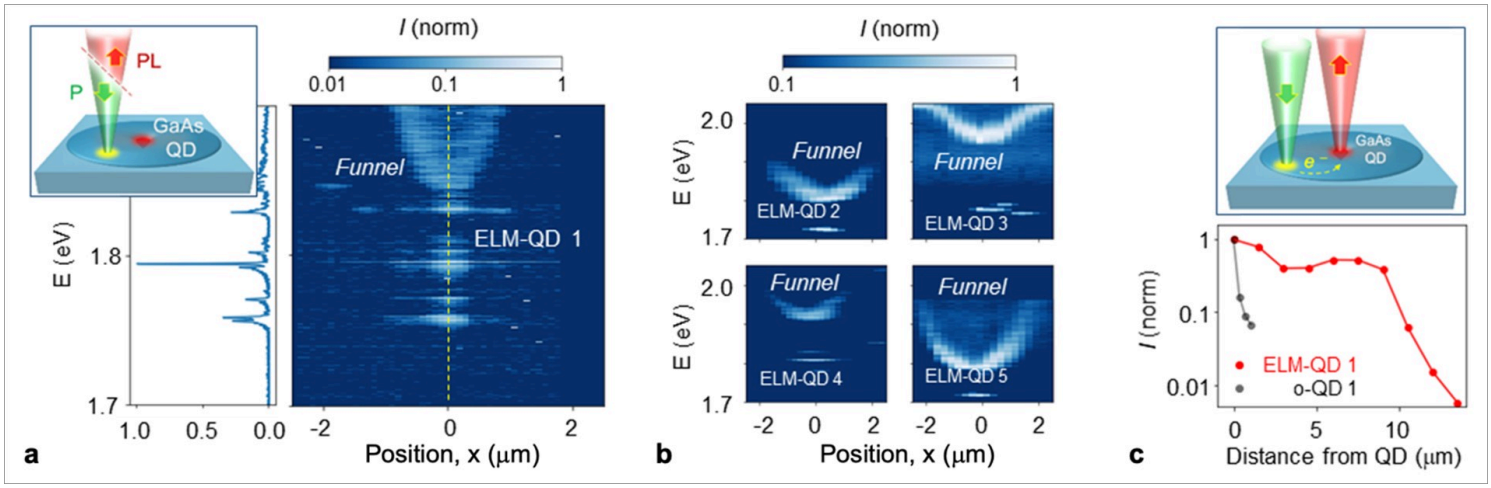

Figure 3

Photoluminescence (PL) signature of ELM-QD (a) *Main panel:* Spatial distribution of PL for a representative ELM-QD (ELM-QD 1). Micro-PL spectra were measured using an optical excitation beam

of ~1 mm in diameter translated across the surface of the QD sample. The QD position is indicated in the map with a vertical yellow dashed line and the corresponding micro-PL spectrum is shown in the left panel. (b) Micro-PL maps of additional four ELM-QDs. (c) Remote optical excitation of ELM-QDs: normalized PL intensity as a function of the distance from the point of excitation for an ELM-QD and o-QD.

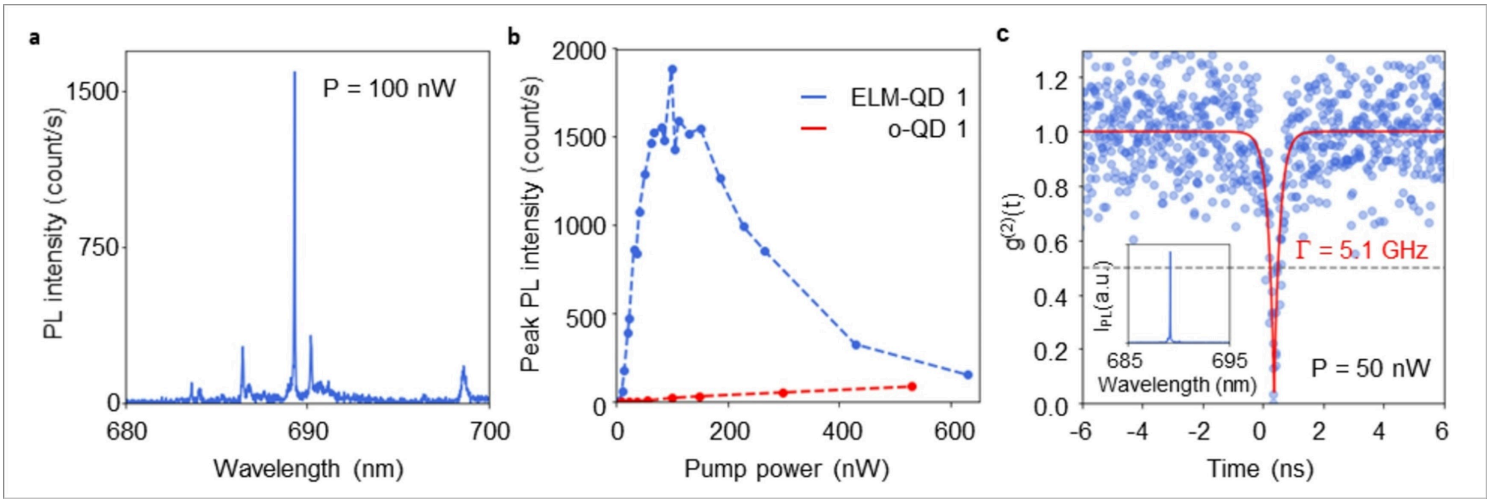

Figure 4

Single-photon emission from ELM-QDs. (a) PL spectrum of the ELM-QD in Fig 3a (ELM-QD 1) pumped with the excitation power of 100 nW. (b) Pump power dependence of the peak PL intensity from ELM-QD (blue) and o-QD (red) (c) Second-order correlation function ($g^{(2)}(t)$) for photon emission from ELM-QD 1. Data are fitted with an exponential decay function, , where A = 0.96 and is 5.1 GHz: *Inset*: filtered ELM-QD PL spectrum.

Supplementary Files

This is a list of supplementary files associated with this preprint. Click to download.

- SupplementaryInformation.docx